

High-mobility, wet-transferred graphene grown by chemical vapor deposition

D. De Fazio^{1(†)}, D. G. Purdie^{1(†)}, A. K. Ott¹, P. Braeuninger-Weimer², T. Khodkov³, S. Goossens³, T. Taniguchi⁴, K. Watanabe⁴, P. Livreri⁵, F. H. L. Koppens³, S. Hofmann², I. Goykhman¹, A. C. Ferrari¹, A. Lombardo^{1*}

¹ Cambridge Graphene Centre, University of Cambridge, Cambridge CB3 0FA, UK

² Department of Engineering, University of Cambridge,

9 J.J. Thomson Avenue, CB3 0FA, Cambridge, UK

³ ICFO-Institut de Ciències Fòniques, The Barcelona Institute of Science and Technology, 08860 Castelldefels (Barcelona), Spain

⁴ National Institute for Materials Science, 1-1 Namiki, Tsukuba 305-0044, Japan

⁵ Università degli Studi di Palermo, 90128 Palermo, Italy and

(†) equal contribution

We report high room-temperature mobility in single layer graphene grown by Chemical Vapor Deposition (CVD) after wet transfer on SiO₂ and hexagonal boron nitride (hBN) encapsulation. By removing contaminations trapped at the interfaces between single-crystal graphene and hBN, we achieve mobilities up to $\sim 70000\text{cm}^2\text{V}^{-1}\text{s}^{-1}$ at room temperature and $\sim 120000\text{cm}^2\text{V}^{-1}\text{s}^{-1}$ at 9K. These are over twice those of previous wet transferred graphene and comparable to samples prepared by dry transfer. We also investigate the combined approach of thermal annealing and encapsulation in polycrystalline graphene, achieving room temperature mobilities $\sim 30000\text{cm}^2\text{V}^{-1}\text{s}^{-1}$. These results show that, with appropriate encapsulation and cleaning, room temperature mobilities well above $10000\text{cm}^2\text{V}^{-1}\text{s}^{-1}$ can be obtained in samples grown by CVD and transferred using a conventional, easily scalable PMMA-based wet approach.

INTRODUCTION

Charge carriers in single layer graphene (SLG) can reach room-temperature (RT) mobility (μ) $> 200000\text{cm}^2\text{V}^{-1}\text{s}^{-1}$ at technologically-relevant carrier densities $n \sim 10^{12}\text{cm}^{-2}$, corresponding to a sheet conductivity $\sigma \sim 30\text{mS}$, with $\sigma = e\mu n$ and e the elementary charge $1.6 \times 10^{-19}\text{C}$ [1], limited by electron-phonon interactions[2, 3]. High $\mu > 10000\text{cm}^2\text{V}^{-1}\text{s}^{-1}$ at such carrier densities is essential for (opto)electronic devices[4], such as microwave transistors[5], photodetectors[6], THz detectors[7] and optical modulators[4, 8]. RT $\mu > 100000\text{cm}^2\text{V}^{-1}\text{s}^{-1}$ can be achieved in micro-mechanically-cleaved (MC) samples, either suspended[9–12] or encapsulated in hexagonal boron nitride (hBN)[13–15]. This is twice that of InSb[13, 16, 17] and InAs[13, 16] at n up to $\sim 4.5 \times 10^{12}\text{cm}^{-2}$ (corresponding to Fermi level $E_F \sim 270\text{meV}$)[2, 13]. Integration of SLG in a foundry requires scalable production and fabrication methods, to meet the requirements for 300mm wafers[4]. Chemical vapor deposition (CVD) allows production of SLG with lateral sizes up to hundreds of meters[18]. A Cu foil is widely used as substrate due to its low carbon solubility (~ 0.005 carbon weight % at 1084°C)[19] and its catalytic role during growth[20, 21]. Polycrystalline continuous films[22, 23] or isolated single crystals[24–27] can be grown by tuning parameters such as partial pressures[28], temperature T [29] or substrate roughness[30, 31].

In order to be integrated into devices, SLG needs then to be removed from Cu and placed onto the target substrate. Several transfer methods have been developed,

classified either as “wet” or “dry”. We consider “wet” all techniques whereby the SLG surface gets in contact with liquids, such water[32], solvents[22, 23] or other chemicals used to remove the substrate[32] at any step of the transfer process. Wet transfer exploits a sacrificial layer (either a polymer[22, 23, 33–37] or a thermal release tape[22]) as support for SLG while the substrate is removed by chemical etching[22, 23, 33], electrochemical delamination[34] or selective interface etching[38]. Wet transfer is simple and easily scalable[22], however it introduces polymer residuals or defects which typically reduce the SLG quality, resulting in undesired doping[35] or low μ ($< 3000\text{cm}^2\text{V}^{-1}\text{s}^{-1}$ [18]). The highest μ at RT reported to date in wet-transferred CVD SLG is $\sim 20000\text{cm}^2\text{V}^{-1}\text{s}^{-1}$ [35, 37], achieved by placing SLG onto mechanically exfoliated hBN[35–37]. This is almost one order of magnitude lower than the state of the art in MC samples transferred by stamping[15].

Dry transfer consists in peeling SLG off the substrate without any chemical etching or electrochemical delamination. This exploits the Van der Waals interaction between SLG and hBN[39]. An hBN flake placed on a polymeric stamp is used to pick SLG[39]. The hBN-SLG stack is subsequently stamped onto a second hBN layer, achieving full encapsulation (*i.e.* the entire SLG area is enclosed between two hBN layers), so that SLG is never in contact with any liquid[39]. μ up to $\sim 3 \times 10^6\text{cm}^2\text{V}^{-1}\text{s}^{-1}$ at 1.8K was reported for dry transferred, encapsulated, CVD grown SLG[39], comparable to MC SLG encapsulated in hBN[13–15]. Dry transfer requires Cu oxidation below the SLG surface[39], to weaken the SLG interaction with Cu[39]. However, Cu oxidation can be a time-consuming process (a few days are required for oxidation

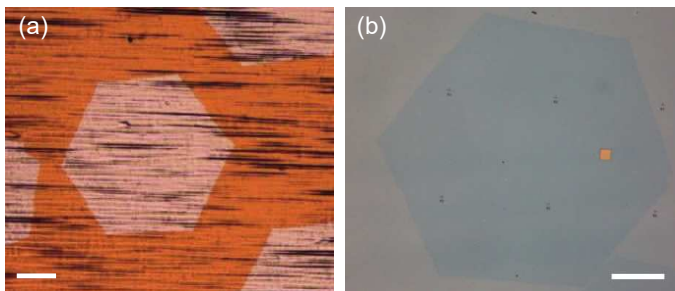


FIG. 1. a) Hexagon-shaped SC-SLG on Cu. Contrast for imaging SC by optical microscopy is enhanced by heating in atmosphere at 250°C for 1 min to promote Cu oxidation. b) SC-SLG wet transferred on SiO_2/Si with patterned lithography markers. Scale bars: $100\mu\text{m}$.

of Cu underneath SLG islands width of few hundred μm at ambient conditions[40]), and its speed depends on the SLG coverage of the Cu foil, as SLG slows oxidation[41].

We reported a method to clean interfaces in heterostructures consisting of MC SLG and hBN[15], achieving atomically-clean interfaces and RT μ up to $\sim 150000\text{cm}^2\text{V}^{-1}\text{s}^{-1}$ even in samples intentionally contaminated with polymers and solvents[15]. Here we apply the same approach to CVD-grown single crystal (SC) SLG domains (lateral size $\sim 500\mu\text{m}$) wet transferred on $\text{Si}+\text{SiO}_2$. We achieve μ up to $\sim 70000\text{cm}^2\text{V}^{-1}\text{s}^{-1}$ at RT and $\sim 120000\text{cm}^2\text{V}^{-1}\text{s}^{-1}$ at 9K, with ballistic transport over $\sim 600\text{nm}$ at 9K. To the best of our knowledge, this is the highest μ reported thus far in wet-transferred, CVD-grown SLG. We also apply the same approach to polycrystalline SLG (poly-SLG) with average grain size of few μm^2 , achieving RT $\mu \sim 7000\text{cm}^2\text{V}^{-1}\text{s}^{-1}$. By then annealing in Ar/H_2 at 600°C we get RT μ up to $\sim 30000\text{cm}^2\text{V}^{-1}\text{s}^{-1}$. Thus, by combining encapsulation and interface cleaning, both SC and poly CVD-grown SLG have RT $\mu \gg 10000\text{cm}^2\text{V}^{-1}\text{s}^{-1}$ even after exposure to contaminants such as etchants, polymers and solvents. Therefore scalable processing methods, such as polymer-based wet transfer, can be used for fabrication of (opto)electronic devices achieving the μ required for them to surpass existing technologies[4].

RESULTS AND DISCUSSION

SLG single crystals are grown on $25\mu\text{m}$ -thick Alfa Aesar, 99.8% purity Cu foil, Fig.1a. As for Ref.42, before growth the Cu foil is floated on the surface of a 30% hydrogen peroxide (H_2O_2) solution at 100°C for 5min to oxidize the back-side. This treatment favours the growth of single crystals due to oxygen-enabled scavenging of carbon impurities trapped in the Cu top surface and bulk, which would otherwise act as nucleation sites during the growth[42]. Growth is then

performed in a Aixtron Black Magic Pro, 4-inch cold wall plasma enhanced-CVD (PECVD) system with a base pressure $\sim 0.05\text{mbar}$. The foil is initially placed in the furnace and heated to $\sim 1065^{\circ}\text{C}$ in a Ar environment (200sccm) at $100^{\circ}\text{C}/\text{min}$. Once the growth T is reached, the Cu foil is annealed keeping T constant in Ar (200sccm) for 30min. Carbon deposition is done in an Ar/H_2 environment (250/26sccm) using 9sccm CH_4 , 0.1% diluted in Ar, for 45min. Samples are then cooled in 250sccm Ar to RT. The crystallinity of the as grown-SLG is confirmed via transmission electron microscopy (TEM)[42]. Electron diffraction on multiple spots reveals the same crystal orientation across the hexagonal SLG domain with $\sim 500\mu\text{m}$ lateral size[42]. SLG crystals are then transferred on $\text{Si}+285\text{nm SiO}_2$ using a wet method[22, 23, 32]. A poly(methyl methacrylate) (PMMA) support layer is spin coated at the SLG surface, following which the samples are placed in a solution of ammonium persulfate (APS) and deionized (DI) water, whereby Cu is chemically etched[22, 23, 32]. The PMMA/SLG stack is then moved to a beaker with DI water to remove APS residuals and lifted with the target SiO_2/Si substrate. After drying, PMMA is removed in acetone, leaving SLG on SiO_2/Si , Fig.1b. We then encapsulate SLG in hBN. hBN bulk crystals are grown as for Ref.43. These are mechanically exfoliated on $\text{Si}+285\text{nm SiO}_2$ to be used for SLG encapsulation. Flakes of lateral size $> 100\mu\text{m}$ are identified and selected by inspecting the SiO_2/Si surface using a combination of bright and dark field optical microscopy, Raman spectroscopy and atomic force microscopy (AFM). For the top hBN we use flakes with thickness $t_{hBN} \sim 2\text{-}300\text{nm}$. For the bottom hBN, flakes with $t_{hBN} > 10\text{nm}$ are chosen, as thinner ones do not screen roughness and charged impurities of the underlying SiO_2 [15, 44].

The encapsulation of SLG in hBN typically results in blisters containing trapped adsorbates and contaminants[45], which must be avoided as they locally degrade transport[45]. Ref.46 showed how to remove contamination blisters by a hot pick-up technique. This uses T above the glass transition, T_g , of the polymer stamp during encapsulation, allowing the interfaces of two materials to be brought together in a directional, conformal manner[46]. We modified this approach by using polycarbonate (PC) stamps at $T = 180^{\circ}\text{C}$, achieving fast ($> 10\mu\text{m}/\text{s}$) removal of contaminants in fully-encapsulated hBN/SLG/hBN heterostructures[15]. This results in atomically-flat interfaces even on samples intentionally contaminated with polymers and solvents, achieving in all cases RT $\mu > 150000\text{cm}^2\text{V}^{-1}\text{s}^{-1}$ [15]. As for Ref.15, here we use a transfer stamp consisting of a PC film on a polydimethylsiloxane (PDMS) block for mechanical support, placed on a glass slide attached to a micro-manipulator, enabling fine ($\sim 1\mu\text{m}$) spatial control in x, y and z. T is set using a heated stage. The process is depicted in Fig.2. It begins by positioning the stamp

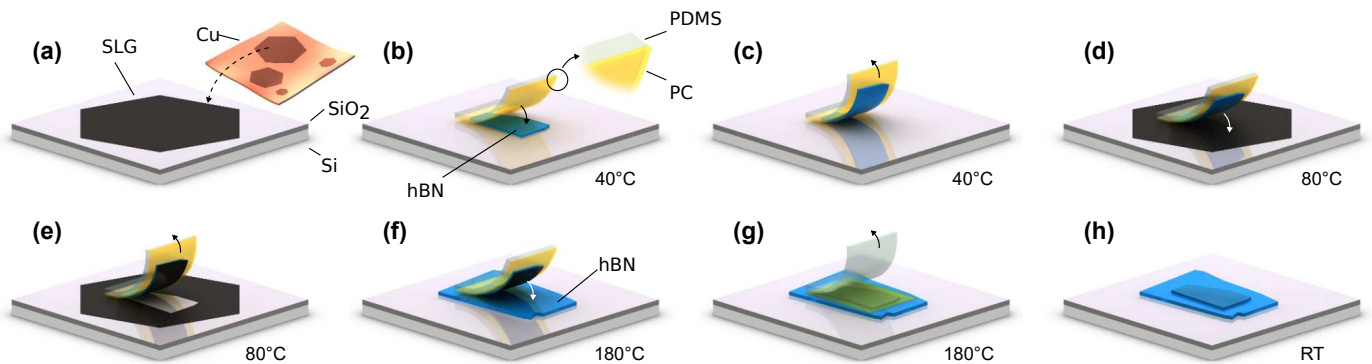


FIG. 2. Transfer process to encapsulate SLG in hBN. (a) SLG (black hexagon) is wet-transferred from Cu to Si+285nm SiO₂. In parallel, (b-c) top hBN (light blue) is picked up with a PC/PDMS stamp (yellow+white). (d-e) SLG is then picked up with the bottom hBN from Si/SiO₂ at 80°C and (f-g) hot-released at 180°C on the bottom hBN, (h) leaving the encapsulated SLG

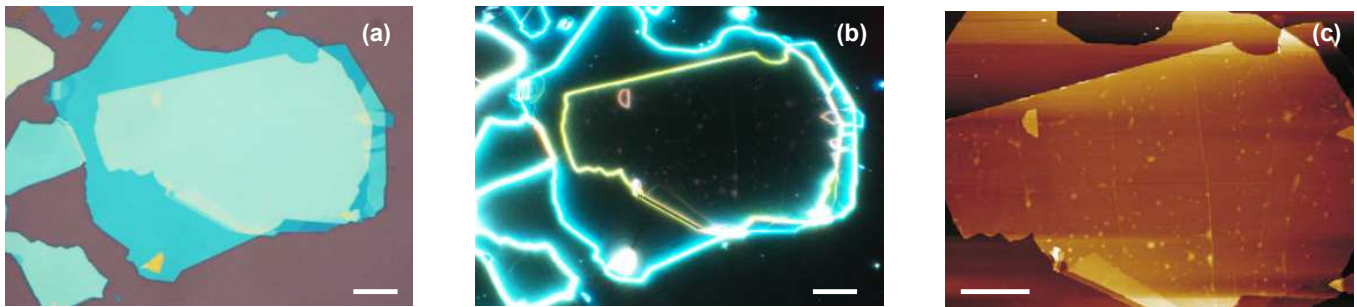


FIG. 3. a) Bright, b) dark field and c) AFM images of SC-SLG encapsulated in hBN. Scale bars 10 μ m

above a hBN flake, then lowering it into contact, with the stage T set to 40°C. As the stamp is withdrawn, the hBN adheres to the PC surface, and is delaminated from SiO₂, Fig.2b,c. The picked-up hBN is then positioned above the (wet transferred) SLG on SiO₂ and brought into contact at 80°C. We then wait \sim 5mins to promote adhesion between hBN and SLG, after which the stamp is lifted, picking up the SLG portion in contact with hBN, Fig.2d,e. The final step consists in bringing the top hBN/SLG into contact with the bottom hBN at 180°C, with the stamp tilted to ensure that contact occurs first on one side, then conformally advancing across the substrate, Fig.2f. At 180°C, withdrawing the stamp releases the PC onto the substrate, Fig.2g, then dissolved by placing the sample in chloroform, Fig.2h. Figs.3a,b are bright and dark field images of the final hBN/SLG/hBN stack. Scans by AFM, Fig.3c, reveal that some blisters are present. They tend to aggregate in specific areas, mostly along vertical lines, which we attribute to residual wrinkles from wet transfer.

The SLG quality is monitored at each step of the fabrication process by Raman spectroscopy. Raman measurements are performed with a Renishaw InVia spectrometer equipped with a 100 \times objective, 2400l/mm grating

at 514nm. The power on the sample is below \sim 1mW to avoid any heating and damage. Fig.4a plots representative spectra of a SC-SLG on Cu (black), after transfer on SiO₂/Si (blue) and encapsulated in hBN (red). The SLG spectrum on Cu is shown after subtraction of the Cu photoluminescence (PL)[47]. This has a 2D peak with a single Lorentzian shape and a with full width at half maximum FWHM(2D) \sim 27cm⁻¹, a signature of SLG[48]. The position of the G peak, Pos(G), is \sim 1588cm⁻¹, with FWHM(G) \sim 14cm⁻¹. The 2D peak position, Pos(2D) is \sim 2706cm⁻¹, while the 2D to G peak intensity and area ratios, I(2D)/I(G) and A(2D)/A(G), are \sim 3 and \sim 5.5. No D peak is observed, indicating negligible defects[49, 50]. After wet transfer on SiO₂/Si, the 2D peak retains its single-Lorentzian lineshape with FWHM(2D) \sim 30cm⁻¹. The D peak is still negligible, indicating that no significant defects are induced by wet transfer. Pos(G) is \sim 1594cm⁻¹, FWHM(G) \sim 11cm⁻¹, Pos(2D) \sim 2692cm⁻¹, I(2D)/I(G) and A(2D)/A(G) are \sim 2.5 and \sim 6.8, indicating a doping $<$ 200meV[51, 52]. After pick up and encapsulation, we perform a Raman mapping over an area \sim 20 μ m \times 30 μ m, using the same measurement conditions. A representative spectrum is shown in red in Fig.4a. This

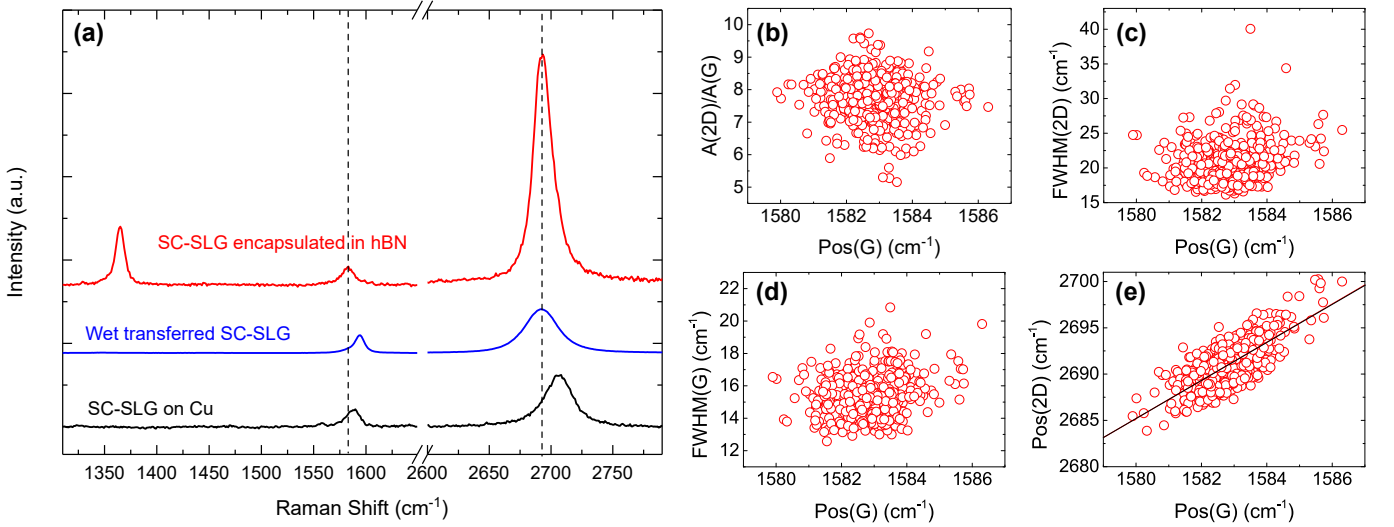


FIG. 4. a) Raman spectra of SC-SLG on Cu (black), transferred on SiO_2 (blue) and after encapsulation (red). In the spectrum on Cu, PL of Cu is subtracted. b,c,d,e) Plots of b) $A(2D)/A(G)$, c) $\text{FWHM}(2D)$, d) $\text{FWHM}(G)$, e) $\text{Pos}(2D)$ a function of $\text{Pos}(G)$ mapped across a $20\mu\text{m} \times 30\mu\text{m}$ region in an encapsulated SC-SLG

comprises both the SLG signatures and the hBN E_{2g} peak $\sim 1364\text{cm}^{-1}$, with $\text{FWHM} \sim 9.5\text{cm}^{-1}$, as expected for bulk hBN[53–55]. The hBN E_{2g} peak is a combination of top and bottom hBN and may overlap a small D peak.

Fig.4b-e plot Raman data extracted from mapping: $A(2D)/A(G)$, $\text{FWHM}(2D)$, $\text{FWHM}(G)$ and $\text{Pos}(2D)$ as a function of $\text{Pos}(G)$. $\text{Pos}(G)$ depends on both doping[51, 52] and strain[56]. This implies that local variations in strain and doping manifest as a spread in $\text{Pos}(G)$ which, in our sample, varies from 1580 to 1586cm^{-1} . The samples have narrow 2D peaks with mean $\text{FWHM}(2D) \sim 20 \pm 3\text{cm}^{-1}$. Figs.4b-d plot $A(2D)/A(G)$ and $\text{FWHM}(G)$ as function of $\text{Pos}(G)$, indicating small variations of both doping and strain within the SLG layer. The mean $A(2D)/A(G)$ is $\sim 7.8 \pm 0.7$, while the mean $\text{FWHM}(G)$ is $\sim 15.4 \pm 1.2\text{cm}^{-1}$. The high $A(2D)/A(G)$ is an indication of intrinsic samples[51], when combined with $\text{FWHM}(G) \sim 15\text{cm}^{-1}$, as well as $\text{Pos}(G) \sim 1583\text{cm}^{-1}$ and $\text{Pos}(2D) \sim 2693\text{cm}^{-1}$ [51].

The rate of change of $\text{Pos}(2D)$ and $\text{Pos}(G)$ with strain is ruled by the Grüneisen parameters (γ)[56], which relate the relative change in the peak positions in response to strain(ϵ), *i.e.* $\gamma = [\omega - \omega_0]/[2\epsilon\omega_0]$, where ω is the frequency of Raman peaks at finite strain and ω_0 the frequency at zero strain[56]. For biaxial strain the Grüneisen parameters for G and 2D peak are respectively $\gamma_G \sim 1.8$ and $\gamma_{2D} \sim 2.6$, resulting in $\Delta\text{Pos}(2D)/\Delta\text{Pos}(G) \sim 2.5$ [56–58]. In the case of uniaxial strain $\gamma_G \sim 1.8$ [56], however extraction of γ_{2D} is not straightforward, as uniaxial strain shifts the relative position of the SLG Dirac cones[56, 58], which in turn affects the 2D peak, as this is involves by intervalley scattering[49, 56]. Ref.[56] experimentally derived an upper bound $\gamma_{2D} \sim 3.55$ and theoretically

calculated $\gamma_{2D} \sim 2.7$, consistent with experimentally reported $\Delta\text{Pos}(2D)/\Delta\text{Pos}(G) \sim 2 - 3$ [56, 59, 60]. Biaxial strain can be differentiated from uniaxial from the absence of G and 2D peak splitting with increasing strain[49], however at low ($\lesssim 0.5\%$) strain the splitting cannot be resolved[56, 59]. Fig.4e shows the correlation between $\text{Pos}(2D)$ and $\text{Pos}(G)$. A linear fit gives a slope $\Delta\text{Pos}(2D)/\Delta\text{Pos}(G) \sim 2.07$. The presence (or coexistence) of biaxial strain cannot be ruled out. For uniaxial(biaxial) strain, $\text{Pos}(G)$ shifts by $\Delta\text{Pos}(G)/\Delta\epsilon \sim 23(60)\text{cm}^{-1}/\%$ [56, 58, 59]. For intrinsic SLG ($E_F \ll 100\text{meV}$), the unstrained, undoped $\text{Pos}(G)$ is $\sim 1581.5\text{cm}^{-1}$ [48, 61]. In Fig.4d the mean $\text{Pos}(G)$ is 1582.8cm^{-1} , which would lead to uniaxial(biaxial) strain $\epsilon \sim 0.05\%(0.02\%)$ [56, 58, 59]. The scattering of $A(2D)/A(G)$ within the mapped area indicates small ($\ll 100\text{meV}$) variation of doping.

We then process our samples into Hall-bars, in order to perform 4-terminal electrical transport. To form contacts, we follow Ref.13. After defining the shape of the desired Hall bar using a hard mask[15], patterned by e-beam lithography, we remove the unmasked part by reactive ion etching (RIE) using a plasma formed from a mix of tetrafluoromethane (CF_4) and oxygen (O_2) (ratio 4:1) under a 20W forward radio frequency (RF) power. SLG is then contacted at its edges[13] by depositing metal leads via e-beam evaporation of 5/70nm Cr/Au.

Fig.5a plots the resistivity of encapsulated CVD SLG as a function of back gate voltage V_{BG} . An optical image of one of the Hall bars is in the inset. The corresponding conductivity is shown in Fig.5b. We extract the field effect mobility $\mu_{FE} = C_{ox}^{-1}(d\sigma/dV_{BG})$ by performing a linear fit to the conductivity close to the charge neutrality point (CNP)[62], where C_{ox} is the gate capacitance

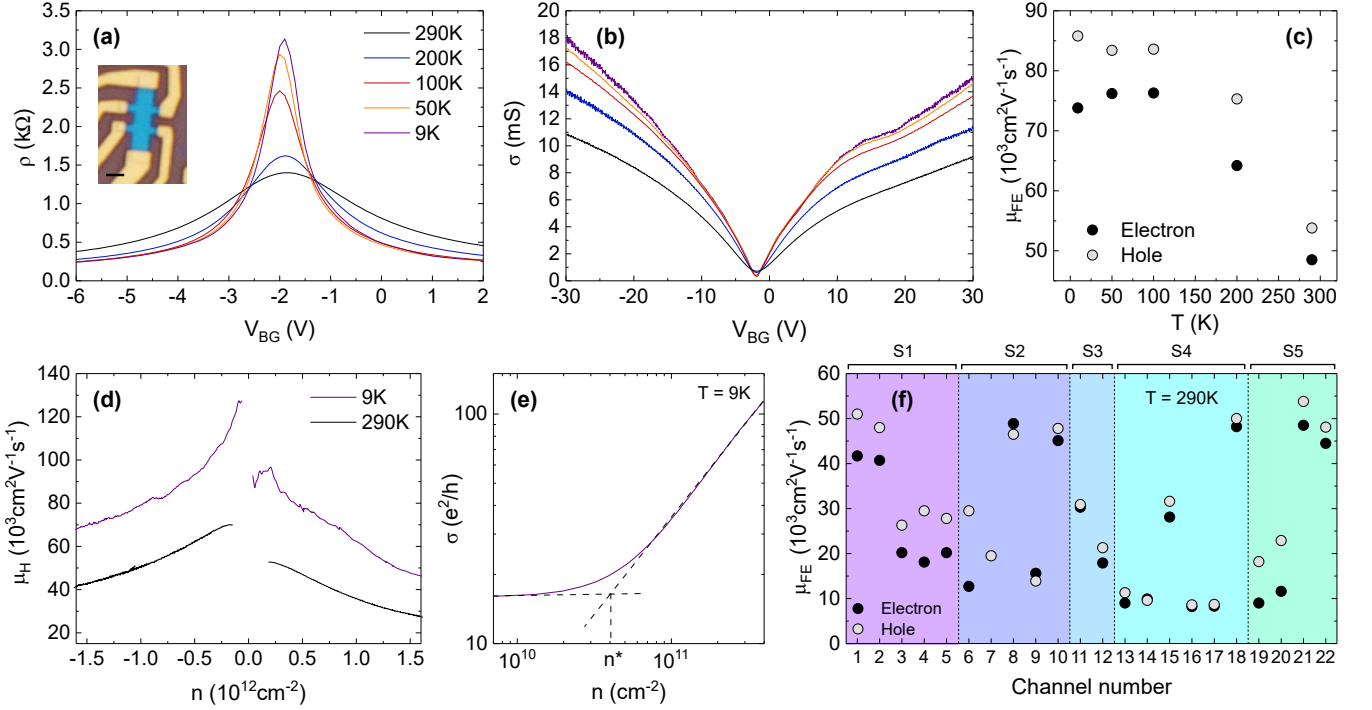


FIG. 5. a) Resistivity as a function of gate voltage between 9 and 290K. Inset: Optical image of the device, with scale bar $1.5\mu\text{m}$. b) Conductivity as a function of gate voltage. c) Field effect mobility as a function of T . d) Density dependent μ from the Drude model $\mu = \sigma/ne$ at 9 and 290K. e) Disorder induced charge inhomogeneity by plotting conductivity as a function of n close to the neutrality point on logarithmic axes. f) Field effect mobility from 22 Hall bars for 5 encapsulated SC-SLG. Each shaded region corresponds to a different sample (S1-S5), while black (grey) dots refer to electron (hole) mobilities in different channels within the same SC-SLG

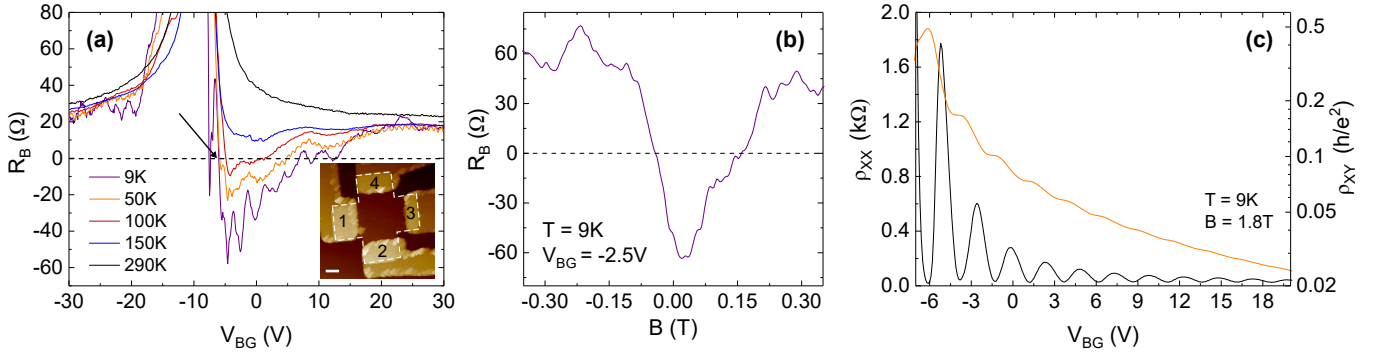


FIG. 6. a) Bend resistance of a Hall cross with arm width 640nm as a function of V_{BG} for $T=9-290\text{K}$. The negative resistance below 100K for positive V_{BG} indicates that carriers travel ballistically from contacts 1 to 3. The arrow indicates $R_B = 0$ at 100K , *i.e.* the transition from diffusive to ballistic transport at which $l_m \sim 640\text{nm}$. Inset: AFM scan of the sample with numbered contacts. Scale bar 200nm . (b) Bend resistance as a function of magnetic field, at $V_{BG} = -2.5\text{V}$ and 9K . (c) ρ_{xx} and ρ_{xy} as a function of V_{BG} at 9K and $B=1.8\text{T}$

per unit area. This is calculated as $\sim 1.1 \cdot 10^{-4} \text{F/m}^2$, assuming a parallel plate capacitor where the bottom hBN is in series with the 285nm SiO_2 layer[15]. The bottom hBN thickness is $\sim 15\text{nm}$ for the sample in Fig.5a. We assume a dielectric constant for hBN $\epsilon \sim 3$, considering that values between 2-4 are usually reported[63]. Our

C_{ox} is orders of magnitude smaller than the quantum capacitance of SLG[64], which is therefore neglected. This yields $\mu_{FE} \sim 49000\text{cm}^2\text{V}^{-1}\text{s}^{-1}$ and $54000\text{cm}^2\text{V}^{-1}\text{s}^{-1}$ for electrons and holes at 290K . μ_{FE} as a function of T in Fig.5c reaches $\sim 86000\text{cm}^2\text{V}^{-1}\text{s}^{-1}$ for holes at 9K .

In order to extract μ as function of n , we investigate

transport in the presence of an out of plane magnetic field B (Hall effect)[1]. To distinguish μ calculated from Hall effect from that estimated from the slope of the conductivity, we indicate the first as μ_H [1]. Assuming a Drude model of conductivity $\mu_H = \sigma/ne$ [1], where n is extracted by measuring the Hall voltage with $B=0.5T$. μ_H in Fig.5d reaches $\sim 70000cm^2V^{-1}s^{-1}$ close to the CNP, while it is $> 30000cm^2V^{-1}s^{-1}$ for n up to $\sim 1.5 \cdot 10^{12}cm^{-2}$. At 9K μ_H is $> 120000cm^2V^{-1}s^{-1}$.

Such values are consistent with those reported in CVD-grown SLG encapsulated in hBN using dry techniques[39, 65]. *E.g.*, Ref.39 measured in Hall bars made with CVD SLG encapsulated by dry transfer in hBN $\mu_{FE} \sim 110000 - 350000cm^2V^{-1}s^{-1}$ at 1.6K. The wet transfer method in Ref.[36] resulted in μ_{FE} up to $\sim 50000cm^2V^{-1}s^{-1}$ at 1.6K[36], ~ 2.5 lower than here.

Fig.5a shows that our SLG is nearly intrinsic, since the resistivity peak occurs close to zero gate voltage, at $V_{CNP} = -1.8V$, indicating moderate $n \sim 1.2 \cdot 10^{11}cm^{-2}$, in agreement with the Raman analysis. Furthermore, the resistivity peak is narrow, with FWHM $\sim 1V$ at 9K. This places an upper bound on the disorder induced charge inhomogeneity, n^* , with narrower peaks corresponding to lower disorder[9, 45, 66]. $n^* < 10^{11}cm^{-2}$ is typically associated with either suspended[66], or dry encapsulated samples[15, 39]. We extract n^* for our sample as for Refs.10, 66, Fig.5e, and get $\sim 4 \cdot 10^{10}cm^{-2}$, one order of magnitude higher than clean MC samples[15].

In order to investigate the μ variation, we fabricate 22 Hall bars from 5 encapsulated SC-SLG. The distribution of μ_{FE} at RT in Fig.5f ranges from a minimum $\sim 10000cm^2V^{-1}s^{-1}$ up to $\sim 55000cm^2V^{-1}s^{-1}$. Bend resistance measurements as a function of T are typically used to probe ballistic transport in SLG[13–15, 39], whereby current is injected around a bend while measuring the voltage. In SLG the carrier mean free path l_m is related to conductivity[67]:

$$l_m = \frac{h}{2e^2\sigma} \sqrt{\frac{1}{\pi n}} \quad (1)$$

where h is the Planck constant. l_m can be extracted from Fig.5a. It varies from $\sim 0.6\mu m$ at 290K up to $\sim 1\mu m$ at 9K. For such l_m we expect ballistic transport[14]. We therefore fabricate a Hall cross with arm width $W = 640nm$ to perform bend resistance measurements as a function of T [13, 14, 65].

An AFM scan of the Hall cross is in the inset of Fig.6a. A constant current $I_{1,2}$ is passed between contacts 1 and 2, and the voltage between contacts 3 (V_3) and 4 (V_4) measured, from which $R_B = (V_4 - V_3)/I_{1,2}$ is extracted. In the diffusive regime, where $l_m < W$, a positive R_B is measured, related to the sheet resistance via the Van der Pauw formula[68]: $\rho = (\pi/\ln 2) R_B$. Alternatively, if $l_m \geq W$, carriers injected at contact 1 follow ballistic trajectories to contact 3, resulting in $R_B < 0$. R_B as a function of T is in Fig.6b. Below 100K, R_B becomes

negative for positive V_{BG} , indicating $l_m \geq 640nm$. At the transition from the diffusive to ballistic $R_B = 0$ and $l_m \sim W$, from which μ may be estimated rearranging Eq.1 by substituting $l_m = W$, to give[14]:

$$\mu \sim \frac{2e}{h} W \sqrt{\frac{\pi}{n_{th}}} \quad (2)$$

where n_{th} is the carrier concentration at which $R_B = 0$. At 9K, $R_B = 0$ occurs at $V_{BG} = -5.8V$, as shown by the arrow in Fig.6a, corresponding to $\mu \sim 129000cm^2V^{-1}s^{-1}$, in agreement with the peak μ_H from Fig.5d. Further confirmation of ballistic transport is achieved by applying an out of plane B , which results in the bending of electrons from their straight-line trajectories, deflecting them away from contact 3, and switching R_B from negative to positive, Fig.6b. Magneto-transport at $B=1.8T$ and 9K, Fig.6c, shows resolved Landau levels, consistent with Refs.36, 39, proving the high electronic quality of our samples.

For all our samples $l_m \lesssim 1\mu m$ at 9K, even in Hall bars with channel widths $> 3\mu m$. This is supported by the fact that Hall crosses with width $W = 1\mu m$ exhibit no negative bend resistance at any T . Our maximum $l_m \sim 1\mu m$ is lower than dry transferred samples, in which l_m typically exceeds the sample dimensions at low T [13, 65], resulting in edge scattering limited conductivity. Indeed, the highest reported l_m in literature are $> 10\mu m$ [13, 65], over an order of magnitude larger than here. However, we note that l_m is not a limiting factor at RT, where μ is limited by electron-phonon scattering[2, 3, 69].

In order to investigate the effect of grain boundaries on μ , we study μ_{FE} of Poly-SLG, CVD-grown, encapsulated in hBN by using the same approach. Due to the small domain size, multiple crystal orientation are present within the same Hall bar. Poly-SLG is grown on $35\mu m$ Cu, following Ref.23. The substrate is annealed in 20sccm H_2 up to $1000^\circ C$ for 30min. Then, 5 sccm of CH_4 is added for the growth to take place for an additional 30 min. The sample is then cooled in vacuum (~ 1.3 mbar) to RT and unloaded from the chamber. SLG is wet transferred onto Si+285nm SiO_2 and then encapsulated in hBN, following the same procedure as above, but with $T=180^\circ C$ in the pick up step, as higher T is required to pick Poly-SLG from SiO_2 .

The Raman spectra at each stage of the transfer process are shown in Fig.7. Compared to SC-SLG, the Raman parameters are more scattered, *e.g.* the variation of $A(2D)/A(G)$ and $Pos(G)$ is twice that of SC-SLG, indicating inhomogeneous doping. The mean $I(2D)/I(G)$ and $A(2D)/A(G)$ ratio are indeed $\sim 7.2 \pm 2.1$ and $\sim 11.1 \pm 4.1$, respectively, which indicate a mean doping $\sim 100meV \pm 100meV$. $Pos(G)$ in unstrained graphene with such low doping is $\sim 1581.6cm^{-1}$ [60]. In our samples, however, the mean $Pos(G)$ is $\sim 1582.6cm^{-1} \pm 0.9cm^{-1}$, indicating the presence of uniaxial(biaxial) strain between $\epsilon \sim 0.02\%$ (0.05%) and $\epsilon \sim 0.03\%$ (0.09%) [56, 58, 59]. The

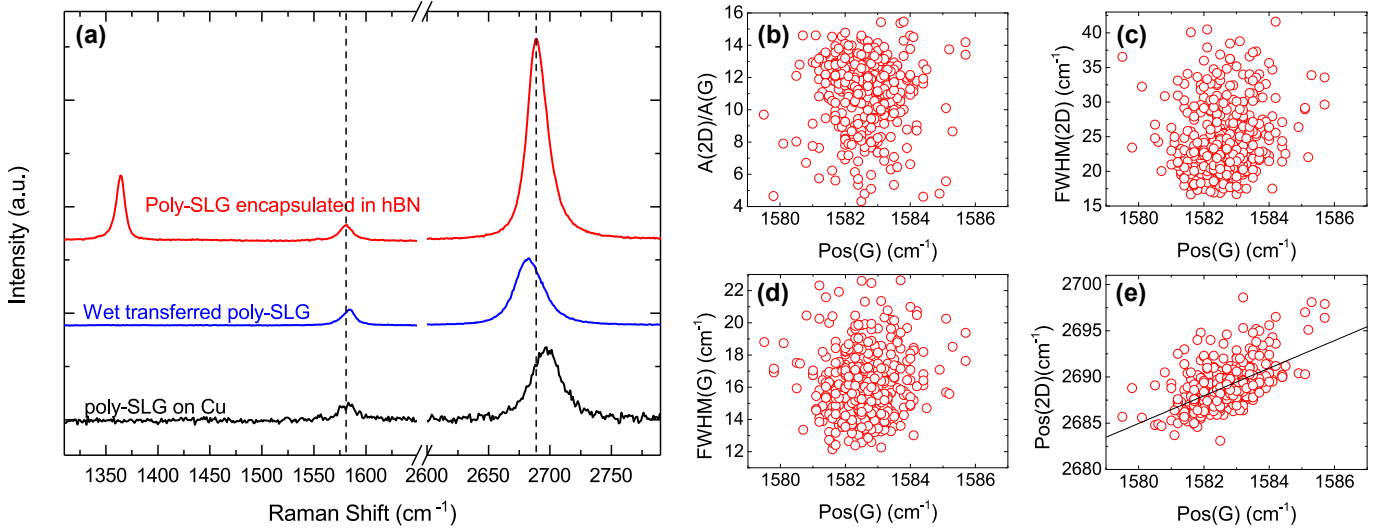


FIG. 7. a) Raman spectra of Poly-SLG on Cu (black), transferred on SiO_2 (blue) and after encapsulation (red). In the spectrum on Cu, PL of Cu has been subtracted. b,c,d,e) plots of b) $A(2D)/A(G)$, c) $\text{FWHM}(2D)$, d) $\text{FWHM}(G)$, e) $\text{Pos}(2D)$ a function of $\text{Pos}(G)$ mapped across a $18\mu\text{m} \times 23\mu\text{m}$ region in an encapsulated Poly-SLG

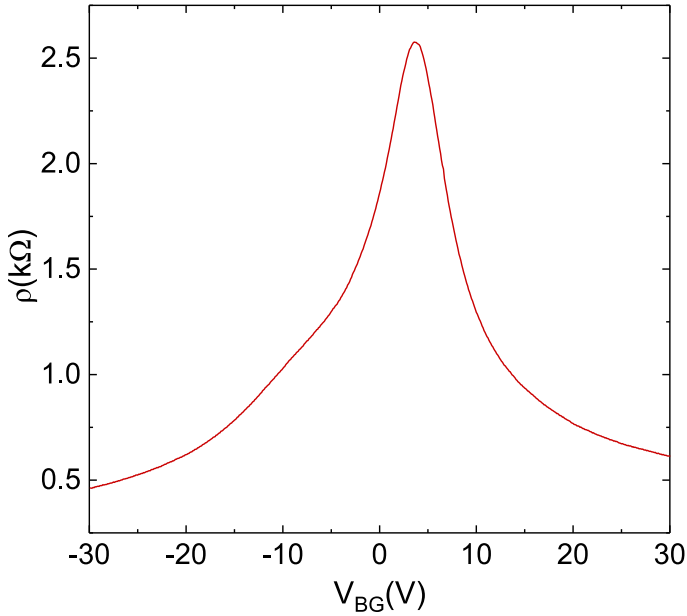


FIG. 8. Resistivity as a function of V_{BG} of Poly-SLG in a Hall bar geometry at 290K.

slope of $\Delta\text{Pos}(2D)/\Delta\text{Pos}(G)$ in Fig.7f is ~ 1.5 lower than in SC-SLG, due to the inhomogeneous distribution of doping and strain in these samples.

The resistivity as a function of V_{BG} is shown in Fig.8. By performing a linear fit to the conductivity close to CNP at $V_{BG} \sim 4\text{V}$, we get $\mu_{FE} = C_{ox}^{-1} (d\sigma/dV_{BG}) \sim 7000\text{cm}^2\text{V}^{-1}\text{s}^{-1}$ and $5000\text{cm}^2\text{V}^{-1}\text{s}^{-1}$ for electrons and holes respectively at 290K. These values are one order of magnitude lower compared to SC-SLG, as expected from the presence of grain boundaries. The shoulder in the left

hand side of the resistivity as a function of V_{BG} at $V_{BG} \sim -8\text{V}$ suggests the presence of an additional CNP in the SLG channel, indicating inhomogeneous doping[70], in good agreement with the Raman analysis.

As μ in Poly-SLG is significantly lower than SC-SLG, we investigate the combined effect of thermal annealing and encapsulation in Poly-SLG. To do so, we first exfoliate hBN onto Si+285nm SiO_2 . Poly-SLG is then transferred to Si+285nm SiO_2 using the polymer-based wet transfer detailed above[22, 23, 32]. This results in SLG partially on SiO_2 and partially on exfoliated hBN. The samples are then annealed at 600°C in Ar/H_2 (40/40sccm). Spatially-resolved Raman spectra are acquired before and after annealing, both on SLG on SiO_2 and on hBN. The annealing sharpens $\text{FWHM}(2D)$ from a mean ~ 27 to ~ 23 after annealing, Fig.9a. This suggests that annealing makes the sample more homogeneous in terms of doping/strain by aggregating adsorbates/contaminants in blisters as shown in Fig.9b. The annealed SLG is then encapsulated by depositing a second hBN using a polymer stamp following Ref.46. Samples are then shaped into Hall bars and contacted using Ni/Pd electrodes (30/40nm). Fig.9c plots the resistance as function of gate. Fig.9d shows μ_{FE} in annealed and encapsulated Poly-SLG, indicating a peak $\mu_{FE} \sim 30000\text{cm}^2\text{V}^{-1}\text{s}^{-1}$, showing that annealing improves μ_{FE} by a factor ~ 5 . We note that this is amongst the highest RT μ_{FE} claimed for Poly-SLG to date.

CONCLUSIONS

We reported high mobility in CVD grown, single crystal SLG placed on Si+ SiO_2 using wet transfer and

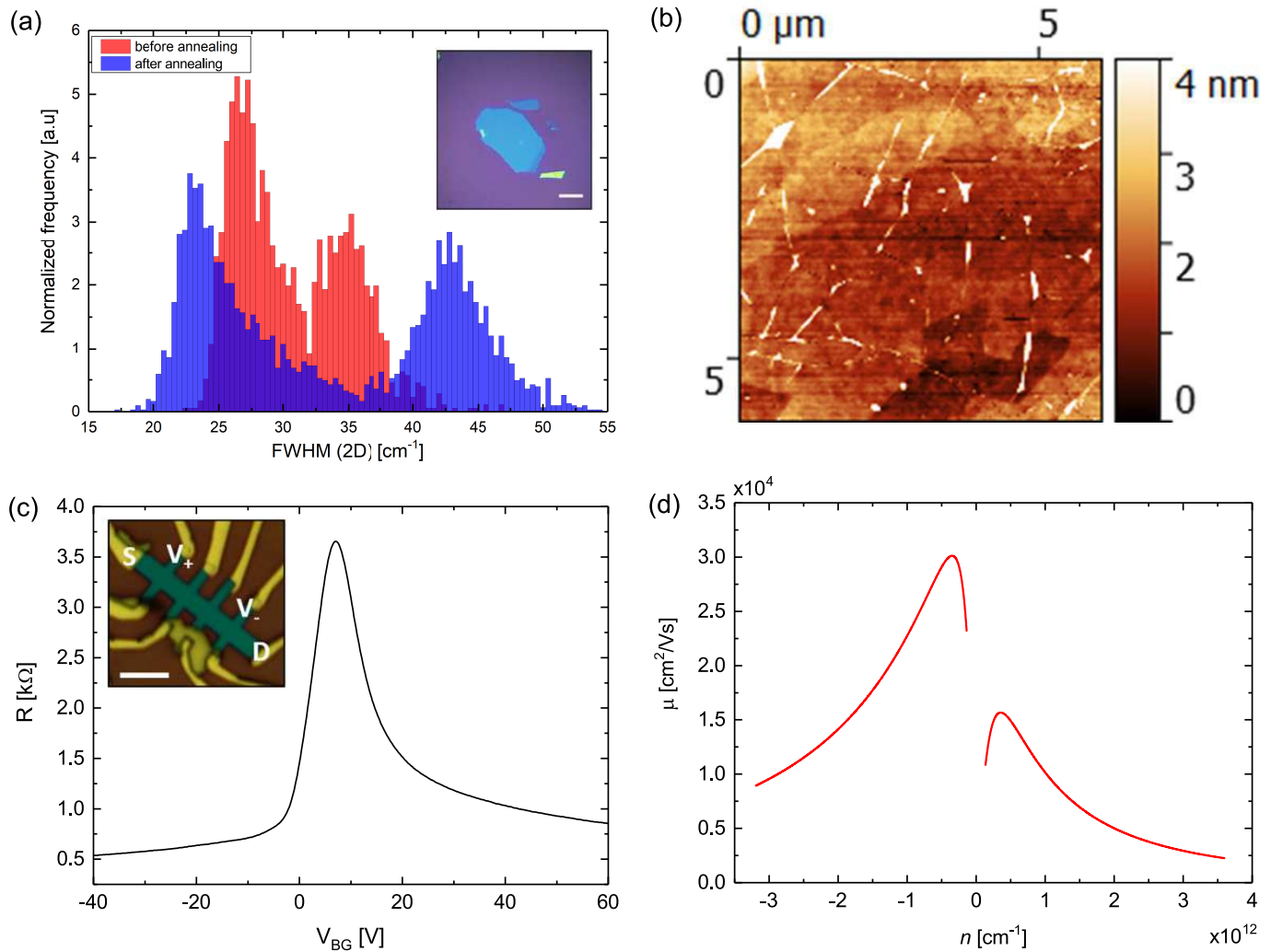


FIG. 9. (a) Statistical distribution of FWHM(2D) for poly-SLG on hBN (blue) before and (red) after annealing in H_2/Ar at 600°C . Spatially-resolved Raman spectra are acquired by mapping Poly-SLG layers partially on SiO_2 and partially encapsulated in hBN. The inset shows the sample mapped, scalebar $10 \mu\text{m}$. b) AFM image of poly-SLG on hBN after annealing. c) four-terminal resistance of annealed and encapsulated poly-SLG as function of V_{BG} . (Inset) Optical picture of the device, scale bar $5 \mu\text{m}$. The bias is applied between (S) source and drain (D) electrodes and the voltage drop along the sample is sensed between V+ and V-. d) μ_{FE} as function of n , extracted by assuming a Drude model for the conductivity

subsequently encapsulated in hBN. By cleaning interfaces between SLG and hBN at $\sim 180^\circ\text{C}$, we achieved mobilities up to up $\sim 70000 \text{ cm}^2 \text{ V}^{-1} \text{ s}^{-1}$ at RT and $> 120000 \text{ cm}^2 \text{ V}^{-1} \text{ s}^{-1}$ at 9K, comparable to values achieved via dry transfer. The samples show ballistic transport over $\sim 600 \text{ nm}$ at 9K. This confirms that encapsulation in hBN and interface cleaning enable high mobility even after conventional polymer-based wet transfer techniques. We also investigated the combined effect of annealing and encapsulation in polycrystalline SLG, achieving RT mobilities up to $\sim 30000 \text{ cm}^2 \text{ V}^{-1} \text{ s}^{-1}$. Our results show that a scalable process such as wet-transfer can be used for the assembly of high-performance devices where high mobility ($> 10000 \text{ cm}^2 \text{ V}^{-1} \text{ s}^{-1}$) is essential.

ACKNOWLEDGEMENTS

We acknowledge funding from the EU Graphene Flagship, ERC Grant Hetero2D, EPSRC Grants EP/K016636/1, EP/K01711X/1, EP/K017144/1, EP/N010345/1, and EP/L016087/1, Wolfson College Cambridge, the Elemental Strategy Initiative conducted by MEXT and JSPS KAKENHI Grant JP15K21722.

* al515@cam.ac.uk

[1] S. M. Sze and K. K. Ng, *Physics of semiconductor devices*, (John Wiley & Sons, 2006).

- [2] J. H. Chen, C. Jang, S. D. Xiao, M. Ishigami and M. S. Fuhrer, *Nat. Nanotechnol.* **3**, 206 (2008).
- [3] C. Park, N. Bonini, T. Sohier, G. Samsonidze, B. Kozinsky, M. Calandra, F. Mauri and N. Marzari, *Nano Lett.* **14**, 1113 (2014).
- [4] M. Romagnoli, V. Sorianello, M. Midrio, F.H.L. Koppens, C. Huyghebaert, D. Neumaier, P. Galli, W. Templ, A. D’Errico and A.C. Ferrari, *Nat. Rev. Mater.*, **3**, 392-414, (2018).
- [5] Y. M. Lin, C. Dimitrakopoulos, K. A. Jenkins, D. B. Farmer, H. Y. Chiu, A. Grill and P. Avouris, *Science* **327**, 662 (2010).
- [6] F. H. L. Koppens, T. Mueller, P. Avouris, A. C. Ferrari, M. S. Vitiello and M. Polini, *Nat. Nanotechnol.* **9**, 780 (2014).
- [7] L. Vicarelli, M.S. Vitiello, D. Coquillat, A. Lombardo, A.C. Ferrari, W. Knap, M. Polini, V. Pellegrini and A. Tredicucci, *Nat. Mater.* **11** 865 (2012).
- [8] V. Sorianello, M. Midrio, G. Contestabile, I. Asselberghs, J. Van Campenhout, C. Huyghebaert, I. Goykhman, A. K. Ott, A. C. Ferrari and M. Romagnoli, *Nat. Photonics* **12**, 40 (2018).
- [9] K. I. Bolotin, K. J. Sikes, Z. Jiang, M. Klima, G. Fudenberg, J. Hone, P. Kim and H. L. Stormer, *Solid State Commun.* **146**, 351 (2008).
- [10] X. Du, I. Skachko, A. Barker and E. Y. Andrei, *Nat. Nanotechnol.* **3**, 491 (2008).
- [11] K. I. Bolotin, F. Ghahari, M. D. Shulman, H. L. Stormer and P. Kim, *Nature* **462**, 196 (2009).
- [12] A. S. Mayorov, D. C. Elias, I. S. Mukhin, S. V. Morozov, L. A. Ponomarenko, K. S. Novoselov, A. K. Geim and R. V. Gorbachev, *Nano Lett.* **12**, 4629 (2012)
- [13] L. Wang, I. Meric, P. Y. Huang, Q. Gao, Y. Gao, H. Tran, T. Taniguchi, K. Watanabe, L. M. Campos, D. A. Muller, J. Guo, P. Kim, J. Hone, K. L. Shepard and C. R. Dean, *Science* **342**, 614 (2013).
- [14] A. S. Mayorov, R. V. Gorbachev, S. V. Morozov, L. Britnell, R. Jalil, L. A. Ponomarenko, P. Blake, K. S. Novoselov, K. Watanabe, T. Taniguchi and A. K. Geim, *Nano Lett.* **11**, 2396 (2011).
- [15] D. G. Purdie, N. M. Pugno, T. Taniguchi, K. Watanabe, A. C. Ferrari and A. Lombardo, *Nat. Commun.* **9**, 5387 (2018).
- [16] B. R. Bennett, R. Magno, J. B. Boos, W. Kruppa and M. G. Ancona, *Solid State Electron.* **49**, 1875 (2005).
- [17] J. M. S. Orr, A. M. Gilbertson, M. Fearn, O. W. Croad, C. J. Storey, L. Buckle, M. T. Emeny, P. D. Buckle and T. Ashley, *Phys. Rev. B* **77**, 165334 (2008).
- [18] T. Kobayashi, M. Bando, N. Kimura, K. Shimizu, K. Kadono, N. Umez, K. Miyahara, S. Hayazaki, S. Nagai, Y. Mizuguchi, Y. Murakami and D. Hobara, *Appl. Phys. Lett.* **102**, (2013).
- [19] G. A. Lopez and E. J. Mittemeijer, *Scripta Mater.* **51**, 1 (2004).
- [20] X. Li, Y. Zhu, W. Cai, M. Borysiak, B. Han, D. Chen, R. D. Piner, L. Colombo and R. S. Ruoff, *Nano Lett.* **9**, 4359 (2009).
- [21] C. Mattevi, H. Kim and M. Chhowalla, *J. Mater. Chem.* **21**, 3324 (2011).
- [22] S. Bae, H. Kim, Y. Lee, X. F. Xu, J. S. Park, Y. Zheng, J. Balakrishnan, T. Lei, H. R. Kim, Y. I. Song, Y. J. Kim, K. S. Kim, B. Ozyilmaz, J. H. Ahn, B. H. Hong and S. Iijima, *Nat. Nanotechnol.* **5**, 574 (2010).
- [23] X. S. Li, W. W. Cai, J. H. An, S. Kim, J. Nah, D. X. Yang, R. Piner, A. Velamakanni, I. Jung, E. Tutuc, S. K. Banerjee, L. Colombo and R. S. Ruoff, *Science* **324**, 1312 (2009).
- [24] Q. Yu, L. A. Jauregui, W. Wu, R. Colby, J. Tian, Z. Su, H. Cao, Z. Liu, D. Pandey, D. Wei, T. F. Chung, P. Peng, N. P. Guisinger, E. A. Stach, J. Bao, S.-S. Pei and Y. P. Chen, *Nat. Mater.* **10**, 443 (2011).
- [25] X. S. Li, C. W. Magnuson, A. Venugopal, R. M. Tromp, J. B. Hannon, E. M. Vogel, L. Colombo and R. S. Ruoff, *J. Am. Chem. Soc.* **133**, 2816 (2011).
- [26] V. Miseikis, F. Bianco, J. David, M. Gemmi, V. Pellegrini, M. Romagnoli and C. Coletti, *2D Mater.* **4**, 021004 (2017).
- [27] L. Gao, W. Ren, H. Xu, L. Jin, Z. Wang, T. Ma, L.-P. Ma, Z. Zhang, Q. Fu, L.-M. Peng, X. Bao and H.-M. Cheng, *Nat. Commun.* **3**, 699 (2012).
- [28] I. Vlassiouk, M. Regmi, P. Fulvio, S. Dai, P. Datskos, G. Eres and S. Smirnov, *ACS Nano* **5**, 6069 (2011).
- [29] S. Bhaviripudi, X. Jia, M. S. Dresselhaus and J. Kong, *Nano Lett.* **10**, 4128 (2010).
- [30] Z. Yan, J. Lin, Z. Peng, Z. Sun, Y. Zhu, L. Li, C. Xiang, E. L. Samuel, C. Kittrell and J. M. Tour, *ACS Nano* **6**, 9110 (2012).
- [31] H. Wang, G. Wang, P. Bao, S. Yang, W. Zhu, X. Xie and W.-J. Zhang, *J. Am. Chem. Soc.* **134**, 3627 (2012).
- [32] F. Bonaccorso, A. Lombardo, T. Hasan, Z. P. Sun, L. Colombo and A. C. Ferrari, *Mater. Today* **15**, 564 (2012).
- [33] Q. K. Yu, J. Lian, S. Siriponglert, H. Li, Y. P. Chen, and S. S. Pei, *Appl. Phys. Lett.* **93** (2008).
- [34] Y. Wang, Y. Zheng, X. F. Xu, E. Dubuisson, Q. L. Bao, J. Lu and K. P. Loh, *ACS Nano* **5**, 9927 (2011).
- [35] W. Gannett, W. Regan, K. Watanabe, T. Taniguchi, M. F. Crommie and A. Zettl, *Appl. Phys. Lett.* **98**, 242105 (2011).
- [36] N. Petrone, C. R. Dean, I. Meric, A. M. van der Zande, P. Y. Huang, L. Wang, D. Muller, K. L. Shepard and J. Hone, *Nano Lett.* **12**, 2751 (2012).
- [37] V. E. Calado, S. E. Zhu, S. Goswami, Q. Xu, K. Watanabe, T. Taniguchi, G. C. A. M. Janssen and L. M. K. Vandersypen, *Appl. Phys. Lett.* **104**, 023103 (2014).
- [38] R. Wang, P. R. Whelan, P. Braeuninger-Weimer, S. Tappertzhofen, J. A. Alexander-Webber, Z. A. Van Veldhoven, P. R. Kidambi, B. S. Jessen, T. Booth, P. Bggild and S. Hofmann, *ACS Appl. Mater. Interfaces* **8**, 33072 (2016).
- [39] L. Banszerus, M. Schmitz, S. Engels, J. Dauber, M. Oellers, F. Haupt, K. Watanabe, T. Taniguchi, B. Beschoten and C. Stampfer, *Sci. Adv.* **1**, e150022 (2015).
- [40] M. Droegeler, L. Banszerus, F. Volmer, T. Taniguchi, K. Watanabe, B. Beschoten and C. Stampfer, *Appl. Phys. Lett.* **111**, 152402 (2017).
- [41] S. Chen, L. Brown, M. Levendorf, W. Cai, S.-Y. Ju, J. Edgeworth, X. Li, C. W. Magnuson, A. Velamakanni, R. D. Piner, J. Kang, J. Park and R. S. Ruoff, *ACS Nano* **5**, 1321 (2011).
- [42] P. Braeuninger-Weimer, B. Brennan, A. J. Pollard and S. Hofmann, *Chem. Mater.* **28**, 8905 (2016).
- [43] T. Taniguchi and K. Watanabe, *J. Cryst. Growth.* **303**, 525 (2007).
- [44] C. R. Dean, A. F. Young, I. Meric, C. Lee, L. Wang, S. Sorgenfrei, K. Watanabe, T. Taniguchi, P. Kim, K. L. Shepard and J. Hone, *Nat. Nanotechnol.* **5**, 722 (2010).

- [45] A. V. Kretinin, Y. Cao, J. S. Tu, G. L. Yu, R. Jalil, K. S. Novoselov, S. J. Haigh, A. Gholinia, A. Mishchenko, M. Lozada, T. Georgiou, C. R. Woods, F. Withers, P. Blake, G. Eda, A. Wirsig, C. Hucho, K. Watanabe, T. Taniguchi, A. K. Geim *et al.*, *Nano Lett.* **14**, 3270 (2014).
- [46] F. Pizzocchero, L. Gammelgaard, B. S. Jessen, J. M. Caridad, L. Wang, J. Hone, P. Boggild and T. J. Booth, *Nat. Commun.* **7**, 11894 (2016).
- [47] A. A. Lagatsky, Z. Sun, T. S. Kulmala, R. S. Sundaram, S. Milana, F. Torrisi, O. L. Antipov, Y. Lee, J. H. Ahn, C. T. A. Brown, W. Sibbett and A. C. Ferrari, *Appl. Phys. Lett.* **102**, 013113 (2013).
- [48] A. C. Ferrari, J. C. Meyer, V. Scardaci, C. Casiraghi, M. Lazzeri, F. Mauri, S. Piscanec, D. Jiang, K. S. Novoselov, S. Roth and A. K. Geim, *Phys. Rev. Lett.* **97**, 187401 (2006).
- [49] A. C. Ferrari and D. M. Basko, *Nat. Nanotechnol.* **8**, 235 (2013).
- [50] L. G. Cancado, A. Jorio, E. H. Ferreira, F. Stavale, C. A. Achete, R. B. Capaz, M. V. Moutinho, A. Lombardo, T. S. Kulmala and A. C. Ferrari, *Nano Lett.* **11**, 3190 (2011).
- [51] A. Das, S. Pisana, B. Chakraborty, S. Piscanec, S. K. Saha, U. V. Waghmare, K. S. Novoselov, H. R. Krishnamurthy, A. K. Geim, A. C. Ferrari and A. K. Sood, *Nat. Nanotechnol.* **3**, 210 (2008).
- [52] D. M. Basko, S. Piscanec and A. C. Ferrari, *Phys. Rev. B* **80**, 165413 (2009).
- [53] R. Arenal, A. C. Ferrari, S. Reich, L. Wirtz, J. Y. Mevellec, S. Lefrant, A. Rubio and A. Loiseau, *Nano Lett.* **6**, 1812 (2006).
- [54] S. Reich, A. C. Ferrari, R. Arenal, A. Loiseau, I. Bello and J. Robertson, *Phys. Rev. B* **71**, (2005).
- [55] R. J. Nemanich and S. A. Solin, *Phys. Rev. B* **20**, 392 (1979).
- [56] T. M. G. Mohiuddin, A. Lombardo, R. R. Nair, A. Bonetti, G. Savini, R. Jalil, N. Bonini, D. M. Basko, C. Galiotis, N. Marzari, K. S. Novoselov, A. K. Geim and A. C. Ferrari, *Phys. Rev. B* **79**, 205433 (2009).
- [57] J. E. Proctor, E. Gregoryanz, K. S. Novoselov, M. Lotya, J. N. Coleman and M. P. Halsall, *Phys. Rev. B* **80**, 073408 (2009).
- [58] J. Zabel, R. R. Nair, A. Ott, T. Georgiou, A. K. Geim, K. S. Novoselov and C. Casiraghi, *Nano Lett.* **12**, 617 (2012).
- [59] D. Yoon, Y.W. Son and H. Cheong, *Phys. Rev. Lett.* **106**, 155502 (2011).
- [60] J. E. Lee, G. Ahn, J. Shim, Y. S. Lee and S. Ryu, *Nat. Commun.* **3**, 1024 (2012).
- [61] S. Piscanec, M. Lazzeri, A. C. Ferrari and J. Robertson, *Phys. Rev. Lett.* **93**, 185503 (2004).
- [62] K. S. Novoselov, A. K. Geim, S. V. Morozov, D. Jiang, Y. Zhang, S. V. Dubonos, I. V. Grigorieva and A. A. Firsov, *Science* **306**, 666 (2004).
- [63] K. K. Kim, A. Hsu, X. Jia, S. M. Kim, Y. Shi, M. Dresselhaus, T. Palacios and J. Kong, *ACS Nano* **6**, 8583 (2012).
- [64] J. Xia, F. Chen, J. Li and N. Tao, *Nat. Nanotechnol.* **4**, 505 (2009).
- [65] L. Banszerus, M. Schmitz, S. Engels, M. Goldsche, K. Watanabe, T. Taniguchi, B. Beschoten and C. Stampfer, *Nano Lett.* **16**, 1387 (2016).
- [66] N. J. G. Couto, D. Costanzo, S. Engels, D. K. Ki, K. Watanabe, T. Taniguchi, C. Stampfer, F. Guinea and A. F. Morpurgo, *Phys. Rev. X* **4**, 041019 (2014).
- [67] E. H. Hwang, S. Adam and S. Das Sarma, *Phys. Rev. Lett.* **98**, (2007).
- [68] L. J. Van der Pauw, *Philips Res. Rep.* **13**, 1 (1958).
- [69] E. H. Hwang and S. Das Sarma, *Phys. Rev. B* **77**, 115449 (2008).
- [70] P. Blake, R. Yang, S. V. Morozov, F. Schedin, L. A. Ponomarenko, A. A. Zhukov, R. R. Nair, I. V. Grigorieva, K. S. Novoselov and A. K. Geim, *Solid State Commun.* **149**, 1068 (2009).